

Photoelectrochemical Valorization of Biomass Derivatives with Hematite Photoanodes Modified by Cocatalysts

Irene Carrai, Raffaello Mazzaro,* Elena Bassan, Giacomo Morselli, Alberto Piccioni, Silvia Grandi, Stefano Caramori,* Paola Ceroni,* and Luca Pasquini

The solar-driven oxidation of biomass to valuable chemicals is rising as a promising anodic reaction in photoelectrochemical cells, replacing the sluggish oxygen evolution reaction and improving the added value of the energy conversion process. Herein, the photooxidation of 5-hydroxymethylfurfural into furan dicarboxylic acid (FDCA) is performed in basic aqueous environment (borate buffer, pH 9.2), with the addition of 2,2,6,6-tetramethylpiperidine-1-oxyl (TEMPO) as redox mediator. Because of its good stability, cost-effectiveness, and nontoxicity, titanium-modified hematite (Ti:Fe₂O₃) photoanodes are investigated to this aim, and their performance is tuned by engineering the semiconductor surface with a thin layer of Co-based cocatalysts, i.e., cobalt iron oxide (CoFeO_x) and cobalt phosphate (CoPi). Interestingly, the electrode modified with CoPi shows improved efficiency and selectivity toward the final product FDCA. The source of this enhancement is correlated to the effect of the cocatalyst on the charge carrier dynamics, which is investigated by electrochemical impedance spectroscopy and intensity-modulated photocurrent spectroscopy analysis. In addition, the results of the latter are interpreted through a novel approach called Lasso distribution of relaxation time, revealing that CoPi cocatalyst is effective in the suppression of the recombination processes and in the enhancement of direct hole transfer to TEMPO.

energy by clean and waste-free chemical processes.^[1–3] Metal–oxide semiconductors (MOS) are promising materials to be employed in photoelectrochemical cells (PECs) because of their electronic properties, good stability, and light harvesting properties in the visible spectral range. Compared to a purely electrocatalytic approach, a PEC device requires 50–200 times the electrode area of a conventional electrolyzer^[4] to provide the same current due to the limited power of the incident sunlight ($\leq 100 \text{ mW cm}^{-2}$), exacerbating the need for inexpensive, nontoxic materials based on earth-abundant elements.^[5]

The competitiveness of photoelectrochemistry with respect to more conventional hydrogen production technologies (e.g., steam reforming or even dark electrolysis) is yet to be demonstrated from an economic point of view.^[6] A very promising way to increase the economic feasibility of this technology is the replacement of water oxidation to oxygen, a challenging and sluggish process leading to a low-value product, with the oxidation of an organic


species producing added-value compounds.^[7] This photo-electro synthetic approach, which is still at the first stages,^[7] has an extremely broad potential^[8] compared to the thermochemical counterpart, spanning from pollution remediation to synthesis of organic compounds and allowing for improved energy efficiency and chemo-selectivity.^[9]

In the frame of artificial photosynthesis, the oxidation reaction needs to involve an abundant, low-cost, and nontoxic feedstock,

1. Introduction

The conversion of sunlight into energy vectors represents one of the few sustainable solutions to the present energy and climate crisis, favoring the currently pursued transition from fossil fuels to renewable energy sources. In this scenario, photoelectrochemical splitting of water into molecular hydrogen and oxygen is a keystone technology, enabling storage of intermittent solar

I. Carrai, R. Mazzaro, A. Piccioni, L. Pasquini
Department of Physics and Astronomy
University of Bologna
Viale Berti Pichat 6/2, 40127 Bologna, Italy
E-mail: raffaello.mazzaro@unibo.it

 The ORCID identification number(s) for the author(s) of this article can be found under <https://doi.org/10.1002/solr.202300205>.

© 2023 The Authors. Solar RRL published by Wiley-VCH GmbH. This is an open access article under the terms of the Creative Commons Attribution-NonCommercial License, which permits use, distribution and reproduction in any medium, provided the original work is properly cited and is not used for commercial purposes.

DOI: 10.1002/solr.202300205

R. Mazzaro, A. Piccioni, L. Pasquini
Institute for Microelectronics and Microsystems
National Research Council
Via Gobetti 101, 40129 Bologna, Italy

E. Bassan, G. Morselli, P. Ceroni
Department of Chemistry “G. Ciamician”
University of Bologna
Via Selmi 2, 40126 Bologna, Italy
E-mail: paola.ceroni@unibo.it

S. Grandi, S. Caramori
Department of Chemical and Pharmaceutical Sciences
University of Ferrara
Via Luigi Borsari 46, 44121 Ferrara, Italy
E-mail: cte@unife.it

and the oxidized product is required to have an added value in comparison to the starting material. Some examples are 1) the reforming of nonrecyclable plastic waste,^[10–13] such as polyester microfibers and oil-contaminated PET, to valuable organic chemicals such as acetate and formate; and 2) the oxidation of biomass derivatives to useful commodities, as demonstrated in the case of lignin oxidation to valuable aromatic monomers,^[14] vanillin,^[15] or biopolymers.^[16] With respect to the latter approach, the oxidation of 5-hydroxymethylfurfural (HMF), an intermediate in the conversion of 6-carbon sugars into levulinic acid, is emerging as an interesting pathway for the synthesis of one of the top value-added chemicals from biomass, 2,5-furan dicarboxylic acid (FDCA) (**Figure 1**), which is the monomer of a PET-analogue polymer, polyethylene furanoate (PEF), as well as several others utility compounds.^[17] In a seminal paper, Choi et al.^[18] demonstrated extremely efficient electrochemical HMF conversion to FDCA with almost unitary yield and Faradaic efficiency in basic conditions (borate buffer, pH 9.2), by employing 2,2,6,6-tetramethylpiperidine 1-oxyl (TEMPO) as a redox mediator to overcome the sluggish kinetics of HMF oxidation. The authors achieved comparable results with a BiVO₄ photoanode, resulting in a reduction of ≈700 mV in the potential necessary to initiate HMF oxidation. More recently, BiVO₄ photoanodes were modified with cobalt phosphate complexes, referred as CoPi, to improve the selectivity with respect to the competitive oxygen evolution reaction (OER), pointing out the importance of the catalyst surface chemistry to tune the charge transfer pathways.^[19] However, BiVO₄ suffers from limited stability to photocorrosion and the photocurrent response with the addition of a CoPi overlayer drops to values as low as 0.2 mA cm⁻². Direct HMF oxidation in absence of TEMPO was also investigated^[20] by employing BiVO₄ photoanodes in the same conditions, as well as WO₃ for different pH regimes, with the latter displaying high conversion rate, but very limited yield (<1%) of FDCA production.

An alternative photoanodic material is hematite (α -Fe₂O₃), a cheap and nontoxic semiconductor composed by earth-abundant elements. These characteristics make it highly preferable to BiVO₄ because Bi is a critical raw material due to the limited availability on earth crust and the high supply risk indicator.^[21] In addition, hematite displays a wider light-harvesting spectrum^[22] ($E_G \approx 2.1$ eV) and improved stability to photocorrosion in basic environment. However, it is characterized by poor photoelectrochemical properties, such as limited hole diffusion and

charge injection efficiency, typically mitigated by doping and surface heterostructuring, respectively.^[23] In particular, Ti-modified hematite photoanodes were demonstrated by our group to efficiently promote an organic reaction, namely the oxidation of benzylamine to N-benzylidene benzylamine,^[24] with almost unitary Faradaic efficiency and photocurrent up to 1.2 mA cm⁻², with the simultaneous production of hydrogen in the cathodic compartment by applying an external bias as low as 0.6 V versus RHE. More recently, hematite photoanodes were reported to efficiently promote HMF oxidation with the addition of TEMPO as electron-mediator,^[25] highlighting a pH-dependent mechanism. The best results were achieved at pH > 12.5 (99.2% HMF conversion to FDCA, with a yield of >90%) but, under these highly alkaline conditions, the degradation of HMF into humin can occur.^[26] In addition, in absence of a large excess of TEMPO, conversion rate and FDCA yield are strongly hampered suggesting a lack of selectivity toward TEMPO oxidation in the proposed conditions.

In the present work, Ti-modified hematite (Ti:Fe₂O₃) photoanodes are employed to catalyze TEMPO-mediated HMF oxidation to FDCA in a two-compartment PEC cell, working in mildly basic aqueous conditions (pH 9.2) to prevent HMF degradation. The addition of Co-based cocatalysts on the surface of Ti:Fe₂O₃ photoanodes is investigated, namely cobalt iron oxide (CoFeO_x) and CoPi. The rationale behind the choice of the cocatalysts lies in the idea to investigate the specific role of the cocatalyst on the competing biomass and water oxidation processes, by comparing the results achieved with an excellent OER catalyst, such as an extremely thin CoFeO_x layer^[27] and a poor one, a thick (≈100 nm) CoPi layer, known to induce a detrimental effect on the charge transfer properties of hematite photoanodes.^[28] The latter is observed to produce enhanced Faradaic efficiency toward HMF oxidation and increased selectivity toward the final product (FDCA) of the multistep oxidation path (**Figure 1**). An in-depth analysis of the charge mobility properties of hematite photoanodes is also carried out by intensity-modulated photocurrent spectroscopy (IMPS) and electrochemical impedance spectroscopy (EIS) and compared to the catalyst-modified photoelectrodes. In particular, a newly developed algorithm for the analysis of IMPS data, based on the DRT analysis, is implemented for the first time to enable a correlation between charge carrier dynamics at the semiconductor/electrolyte interface and the reaction selectivity.

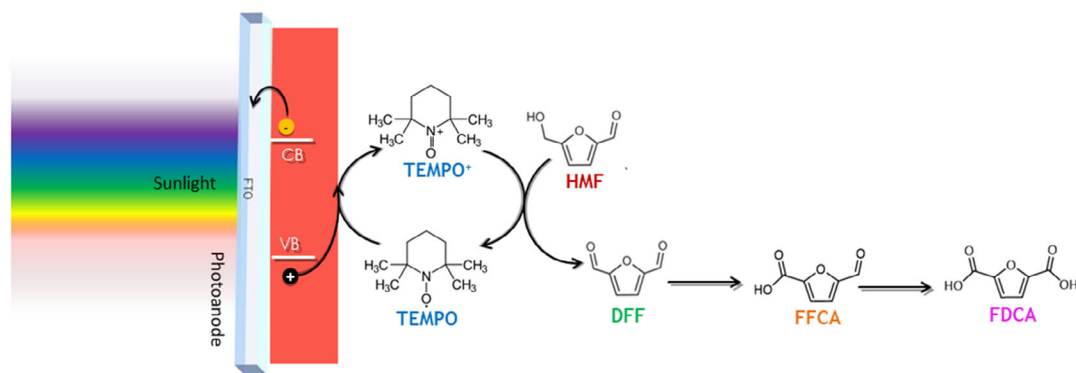


Figure 1. Favored reaction pathway at pH < 12.5 of the TEMPO-mediated HMF oxidation to FDCA.

2. Results and Discussion

The synthetic approach for the preparation of the $\text{Ti:Fe}_2\text{O}_3$, as well as the modification procedure with the cocatalysts (i.e., CoPi and CoFeO_x), was adapted from previously reported literature^[29,30] and described in detail in the experimental section. The examination on the structural, morphological, and optical properties is here reported, followed by a discussion on the stability and photoelectrochemical performances of these photoanodes.

2.1. Structure, Morphology, and Optical Properties

Pristine $\text{Ti:Fe}_2\text{O}_3$ photoanodes display a homogeneous microstructure characterized by thin film islands with a lateral width of 2–5 μm , separated by thermal stress-induced cracks in the film resulting from the fast thermal annealing process. As displayed by scanning electron microscopy (SEM) analysis (Figure 2a), the surface of the islands is composed of sintered nanoparticles with a diameter in the 20–30 nm range. The cross-section of the $\text{Ti:Fe}_2\text{O}_3$ thin film highlights the presence of columnar structures with a uniform thickness in the range 1.5–1.7 μm . Energy-dispersive spectrometry (EDS) analysis clearly displays the homogeneous distribution of Fe and O on the underlying tin oxide film, as well as the presence of titanium throughout the entire hematite film thickness, with a slight increase at the very surface

of the electrode. This is compatible with a certain degree of porosity of the structure, allowing for the penetration of the Ti(IV) precursor within the hematite layer. The high-temperature annealing then promotes the diffusion of Ti(IV) in the hematite lattice, but also results in the formation of the cracked morphology in the thick hematite layer, which may have a beneficial effect on the PEC activity due to the increase of surface area exposed to the electrolyte.

Interestingly, nanoscale analysis of the electrode by high-resolution transmission electron microscopy (HR-TEM) (Figure 2b) reveals the presence of crystalline sub-10 nm nanoparticles, whose lattice is compatible with rutile TiO_2 . Further confirmation is given by the XRD analysis of Figure 2c where, in addition to the Bragg reflections of hematite and FTO, broad peaks associated to rutile phase appear, confirming its ultrafine crystallite size. This feature is not surprising due to the high average Ti content ($\text{Ti/Fe} = 15 \text{ at}\%$) exhibited by SEM analysis (Figure S1, Supporting Information). The rutile and hematite phases appear finely mixed at the nanoscale, as both elements are always detected by local EDS analysis in different spots of the sample (Figure S2, Supporting Information). The near-surface regions are strongly enriched in Ti, whereas the inner parts exhibit a composition closer to the average value. Since the solubility limit of Fe in TiO_2 is low (<1 at%), the detection of abundant Fe in the rutile-rich surface regions may indicate the simultaneous presence of mixed Fe–Ti oxides, with composition akin to ilmenite FeTiO_3 and/or pseudo-brookite Fe_2TiO_5 .

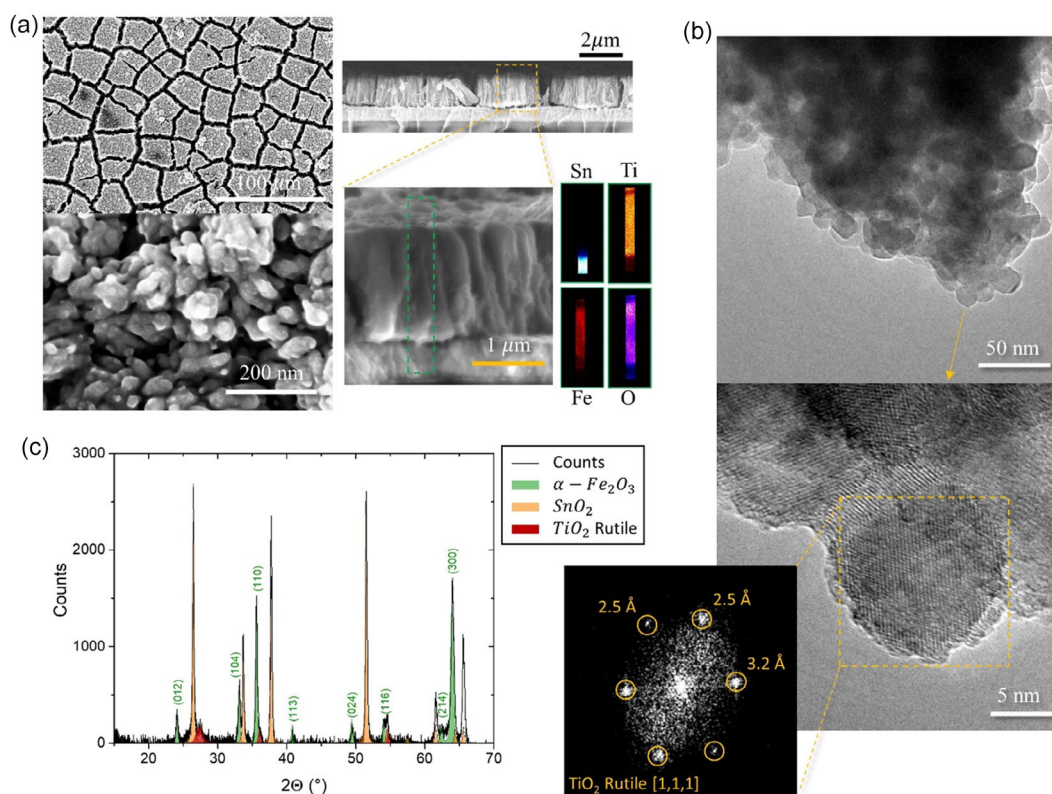


Figure 2. a) Planar (left) and cross-section (right) characterization of a $\text{Ti:Fe}_2\text{O}_3$ photoanode morphology and composition by SEM and EDS analysis; b) HR-TEM analysis of the same photoanode and resulting FFT in the inset; c) XRD analysis after background subtraction, with the corresponding hematite main indexed peaks.

These phases may be difficult to observe by XRD and HR-TEM due to poor crystallinity and lattice spacings close to hematite, but have been reported in previous studies carried out by X-ray absorption spectroscopy, a probe sensitive to the local environment.^[31] This complex structure results in a significant improvement of the typical photocurrent characteristics, in comparison to the one exhibited by pristine Fe_2O_3 photoanodes (Figure S3, Supporting Information).

Conformal deposition of cobalt-based cocatalysts was performed by following previously developed methods, reported multiple times in literature. In particular, CoPi and CoFeO_x thin films were deposited on $\text{Ti:Fe}_2\text{O}_3$ by electrochemical and photoelectrochemical deposition, respectively (Figure 3).^[29,30]

The light harvesting properties of the $\text{Ti:Fe}_2\text{O}_3$ photoanodes are only slightly affected by the overlayer deposition (Figure S4, Supporting Information).

2.2. PEC-OER Characteristics of Cocatalyst-Modified $\text{Ti:Fe}_2\text{O}_3$ Photoanodes

Preliminary characterization of the photoelectrode performance was carried out in a borate buffer solution (0.25 M, pH 9.2), to determine the activity toward OER. Chopped linear sweep

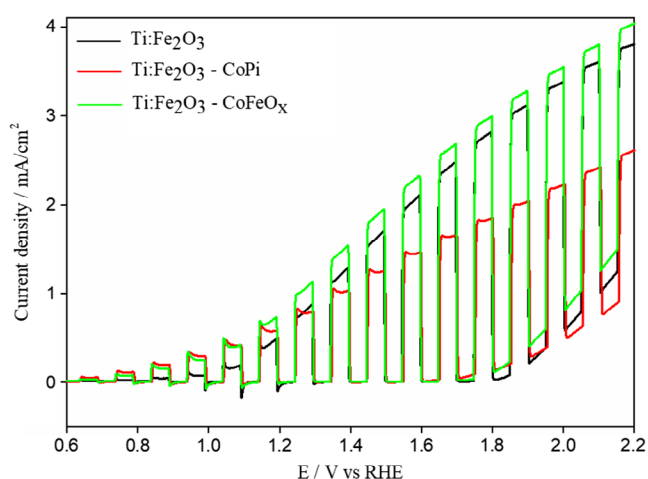


Figure 4. Chopped LSVs for the three electrodes: $\text{Ti:Fe}_2\text{O}_3$ (black line), $\text{Ti:Fe}_2\text{O}_3\text{-CoPi}$ (red line), and $\text{Ti:Fe}_2\text{O}_3\text{-CoFeO}_x$ (green line) in borate buffer (0.25 M, pH 9.2).

voltammetries (LSVs, Figure 4 solid lines) showed that the addition of a cocatalyst results in a decrease of the onset photopotential. However, while the CoFeO_x overlayer produces slightly

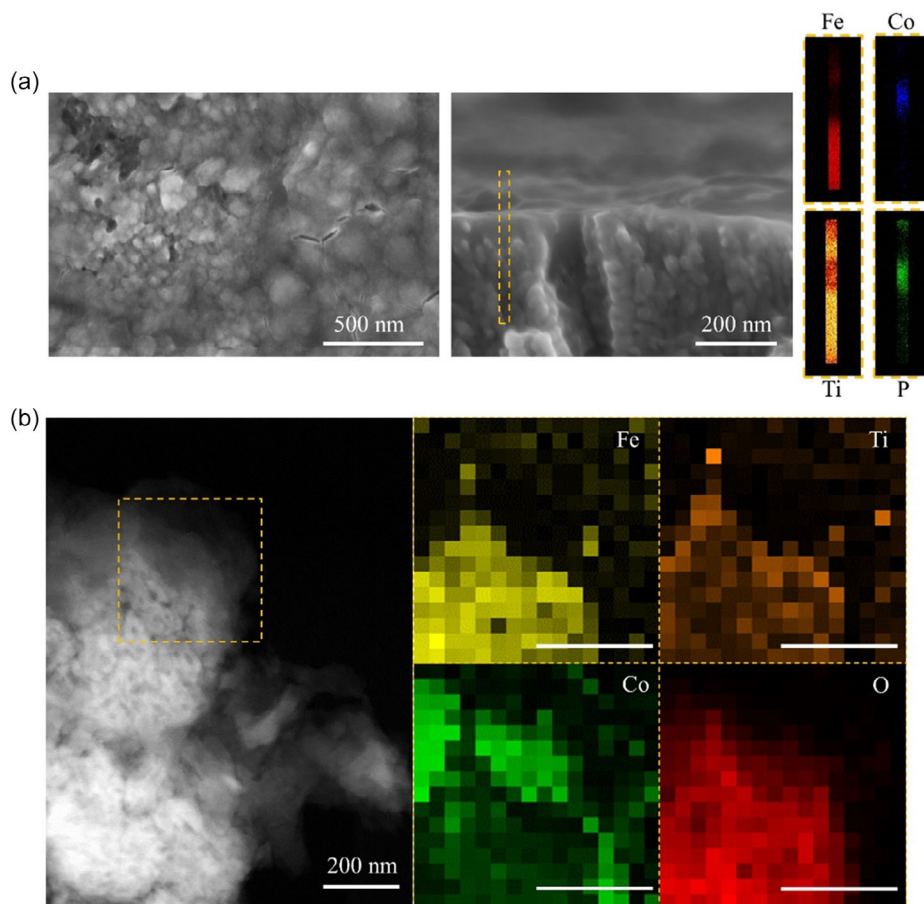


Figure 3. a) Planar (left) and cross-section (right) characterization of a $\text{Ti:Fe}_2\text{O}_3\text{-CoPi}$ photoanode morphology and composition by SEM and EDS analysis; b) STEM micrograph of a detail of the same photoanode and resulting EDS mapping of main representative elements, highlighting the localization of Co-related signal on the surface of the hematite structures.

increased photocurrent, CoPi gives the opposite effect. The limiting photocurrent density is decreased by $\approx 0.4 \text{ mA cm}^{-2}$ at 1.6 V versus RHE, suggesting that the thick CoPi overlayer partially reduces the photoelectrochemical OER rate.

The stability of the photoanodes under long irradiation periods was assessed, by recording LSVs before (continuous line) and after (dashed line) pulsed chrono-coulometries of 37 h (at 1.6 V vs RHE) (Figure S5, Supporting Information): the current/voltage characteristics were very similar in shape and the response of the photoelectrodes was substantially preserved, so that it was possible to use these photoanodes several times, with no loss in terms of performance. The electrochemically active surface area (ECSA) was evaluated by following the previously reported approach,^[32] based on the determination of the anode double-layer capacitance (C_{dl}) from the electrochemical impedance spectrum at E_{OCP} (Figure S6, Supporting Information). C_{dl} is equal to 0.112 mF cm^{-2} for pristine $\text{Ti:Fe}_2\text{O}_3$ and a similar value (0.100 mF cm^{-2}) is obtained for the $\text{Ti:Fe}_2\text{O}_3\text{-CoFeO}_x$ sample. A non-negligible drop to 0.076 mF cm^{-2} is observed for $\text{Ti:Fe}_2\text{O}_3\text{-CoPi}$, pointing out a partial surface passivation. This contributes to explain the lower limiting photocurrents observed with $\text{Ti:Fe}_2\text{O}_3$ covered with a thick CoPi overlayer.

2.3. TEMPO-Mediated Photoelectrochemical HMF Conversion by $\text{Ti:Fe}_2\text{O}_3$ Photoanodes with and Without Cocatalysts

The investigation of the PEC activity toward HMF oxidation was performed in borate buffer (0.25 M, pH 9.2), with TEMPO as electron mediator (Figure 5).

For all samples, almost no alteration of the chopped LSVs can be appreciated upon addition of HMF in the electrolyte solution. In the presence of TEMPO and HMF, the onset photopotentials for $\text{Ti:Fe}_2\text{O}_3$ and $\text{Ti:Fe}_2\text{O}_3\text{-CoFeO}_x$ photoanodes are anticipated and the recombination spikes are reduced, whereas $\text{Ti:Fe}_2\text{O}_3\text{-CoPi}$ is barely affected by its addition, since the photocurrent onset is already more cathodic in pure electrolyte.

The performance of each electrode toward HMF photoconversion was evaluated by performing a long-term pulsed chrono-coulometry. The periodic polarization of the Ti-hematite electrodes at OCP was indeed found to be beneficial for the stability of the electrode response, helping to regenerate the electrodic surface from oxidizing intermediates (i.e., peroxides) produced at the electrode's surface upon positive polarization. In order to limit the reaction time, the experiment was performed at 1.6 V versus RHE. There is no dependence of the catalytic pathway on the applied potential, as later discussed in Section 2.5, in which the charge carrier dynamics are studied over a wide range of potentials.

To monitor the reaction progress, the solution was sampled at times corresponding to collect charges equivalent to 0%, 100%, 150%, and 200% of theoretical HMF conversion, considering the 6-electrons oxidation to FDCA (Figure S7, Supporting Information). These values will be denoted as $Q_{100\%}$, $Q_{150\%}$, and $Q_{200\%}$ for clarity purposes. The solution samples were analyzed by high-performance liquid chromatography (HPLC) (see Supporting Information).

The resulting conversion rates are displayed in Figure 6, and complete consumption of HMF was achieved with all the three photoelectrodes, although with different kinetics. With the

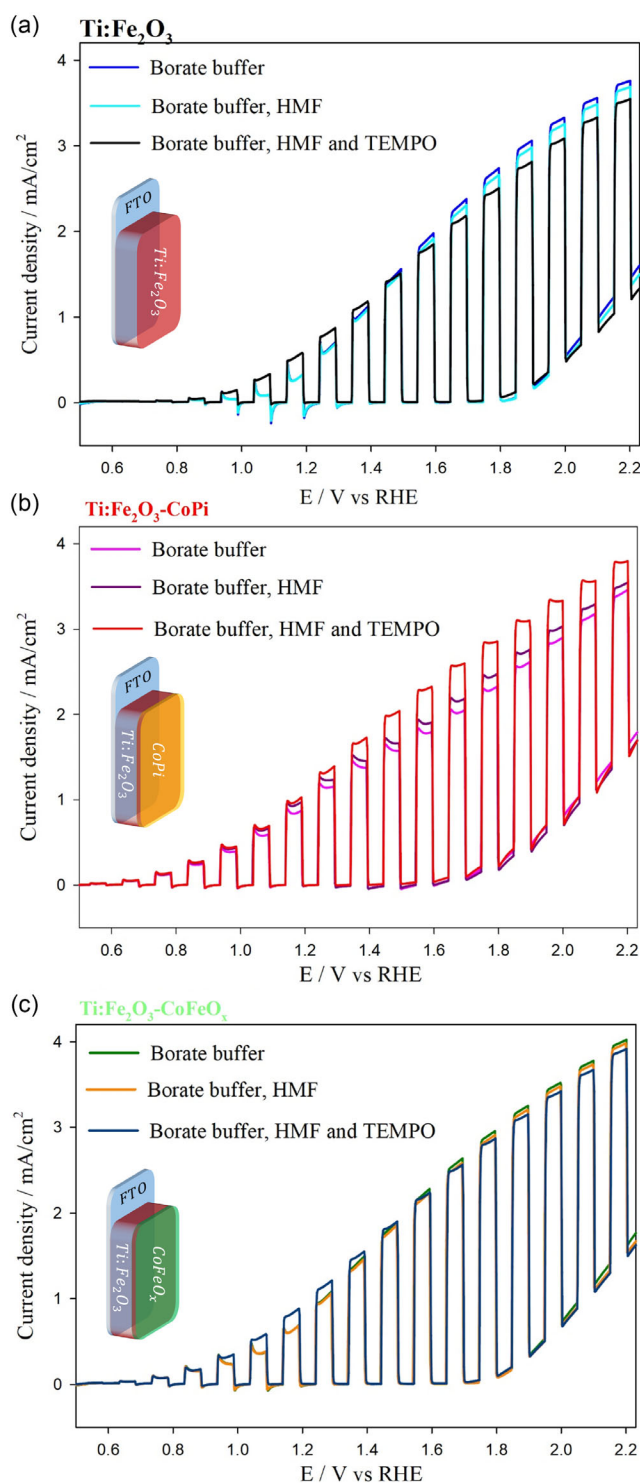


Figure 5. Chopped LSVs of a) $\text{Ti:Fe}_2\text{O}_3$, b) $\text{Ti:Fe}_2\text{O}_3\text{-CoPi}$, and c) $\text{Ti:Fe}_2\text{O}_3\text{-CoFeO}_x$ in borate buffer (0.25 M, pH 9.2), overlaid to those displayed upon the addition of HMF (2.5 mM), or in the presence of both HMF and TEMPO (2.5 and 6.5 mM, respectively).

$\text{Ti:Fe}_2\text{O}_3\text{-CoFeO}_x$ photoanode (Figure 6c), about 50% of HMF remains at $Q_{100\%}$ and the complete disappearance of HMF is observed only at $Q_{200\%}$. The yield for the 6-electrons oxidation

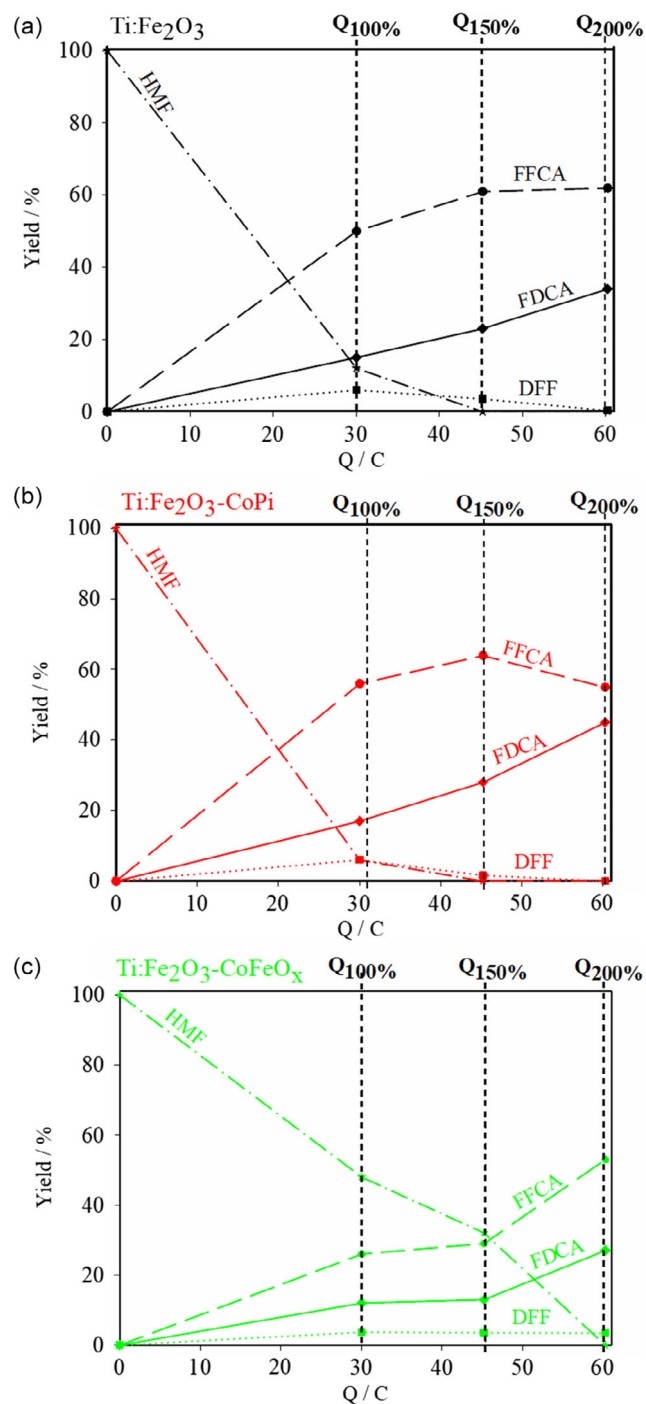


Figure 6. Conversion of HMF and production of its oxidation derivatives as a function of the total charge passed in pulsed chrono-coulometry experiments at 1.6 V versus RHE in borate buffer (0.25 M, pH 9.2) and in the presence of 2.5 mM HMF and 6.5 mM TEMPO: a) Ti:Fe₂O₃, b) Ti:Fe₂O₃-CoPi, and c) Ti:Fe₂O₃-CoFeO_x. Q_{100%} represents the charge corresponding to a theoretical 6-electrons oxidation of HMF to FDCA.

product, i.e., FDCA, is low (around 20%) and starts to increase only at Q_{150%}. This result can be ascribed to a strong competition by the OER when CoFeO_x is employed as the cocatalyst. On the

other hand, pristine Ti:Fe₂O₃ and Ti:Fe₂O₃-CoPi (Figure 6a,b) yield to an almost complete photoconversion of HMF at Q_{100%}, indicating a far better selectivity toward HMF oxidation compared to OER. Accordingly, the Ti:Fe₂O₃ and the Ti:Fe₂O₃-CoPi photoanodes give a similar increase for the formation of FFCA and FDCA up to Q_{150%} (around 45 C). Beyond Q_{150%}, the FDCA content increases, and this effect is more pronounced when CoPi is present on the Ti:Fe₂O₃ surface, suggesting a relevant contribution of the cocatalyst in the last step of HMF photooxidation. It is worth noticing that, in absence of TEMPO, only a minimal fraction of HMF was converted, and DFF was mainly accumulated (Table S1, Supporting Information). This points out the crucial role played by TEMPO as regard both the enhancement of the selectivity toward HMF oxidation and the promotion of the last oxidation step described in Figure 1.

On the contrary, in the presence of TEMPO, the amount of DFF remains very low (<10%) during these photoconversion experiments, in agreement with other literature reports.^[18] It is known that the oxidation of aldehyde to carboxylic acid mediated by TEMPO takes place via the formation of a diol that is favored in basic aqueous environment, according to the mechanism outlined in Figure S8, Supporting Information. Therefore, the conversion of DFF, featuring two aldehyde groups, to FFCA is expected to be fast in the presence of TEMPO and a basic aqueous media. On the other hand, the conversion of FFCA to FDCA is supposed to be slower than the previous one because of the presence of only one aldehyde and of the negative charge of the deprotonated carboxylic group, which hinders the approach of the base OH⁻.

Considering the promising results achieved with the Ti:Fe₂O₃-CoPi photoanode, further investigation on the role of the cocatalyst in the last step of HMF photooxidation, i.e., from FFCA to FDCA was performed. This two-electron oxidation process was followed by repeating the photoconversion experiments in the same conditions using FFCA as substrate and sampling the solutions once the integrated charge corresponding to 100% (Q_{100%}), 200% (Q_{200%}), and 300% (Q_{300%}) of FFCA theoretical conversion was reached. In this case, the aliquots were analyzed via spectrophotometric measurements, being the absorption maxima of the two components located at different wavelengths, i.e., 286 and 263 nm for FFCA and FDCA, respectively (Figure S9, Supporting Information).

Similar to what described in the HMF photoconversion experiment, when HMF was the starting compound (Figure 6a,b), the conversion rate to FDCA is enhanced when CoPi is present as cocatalyst, and the yield for FDCA outperforms the one obtained with bare Ti:Fe₂O₃ for the entire chrono-coulometry (Figure 7).

According to these results, CoPi seems to promote the transfer of the photogenerated hole from the photoelectrode's surface to TEMPO, at the expense of the competitive and multielectron OER.^[19] In this way, even the most challenging and rate-limiting step of the HMF oxidation process,^[18] i.e., FFCA oxidation, can be accelerated. This is further confirmed by calculating the Faradaic efficiency (FE) for the formation of DFF, FFCA, and FDCA during the HMF photoconversion experiment (Figure 6), considering the following equation

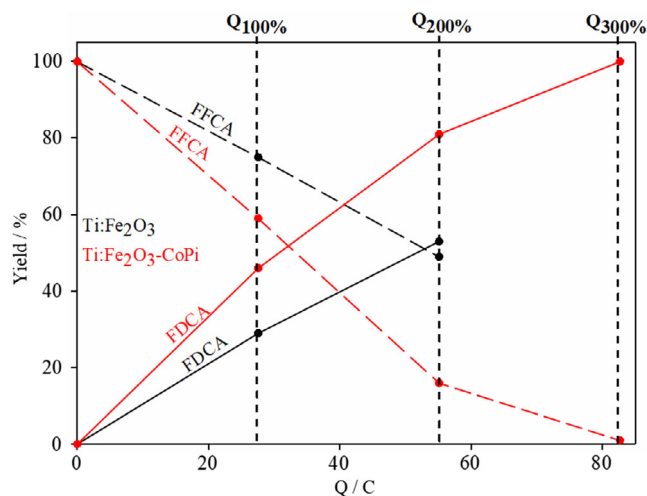


Figure 7. Yield of FFCA (dotted line) and FDCA (continuous line) in pulsed chrono-coulometry experiments at 1.6 V vs RHE in borate buffer (0.25 M, pH 9.2) and in the presence of 6.5 mM FFCA and 6.5 mM TEMPO, for Ti:Fe₂O₃ (black) and Ti:Fe₂O₃-CoPi (red).

$$FE(\%) = n_{\text{mol}} / (Q/nF) \cdot 100 \quad (1)$$

where n_{mol} is the number of moles of product experimentally measured, Q is the cumulative charge passed in the PEC cell during the pulsed-chronocoulometry experiment, F is the Faraday's constant (96.485 C mol⁻¹), and n is the number of electrons exchanged during the oxidative step, i.e., DFF ($n = 2$), FFCA ($n = 4$) and FDCA ($n = 6$). Then, the overall Faradaic efficiency, given by the sum of the Faradaic efficiencies associated to each oxidative intermediate, was determined for $Q_{100\%}$, since the comparison at larger conversion yield would be affected by the reactants consumption.

The resulting FE for pristine Ti:Fe₂O₃, Ti:Fe₂O₃-CoPi, and Ti:Fe₂O₃-CoFeO_x is, respectively, equal to 49%, 55%, and 30%. A large drop in FE is observed when CoFeO_x is employed as cocatalyst, further confirming the inadequacy of CoFeO_x in suppressing OER. On the other hand, CoPi addition is increasing the FE toward HMF oxidation products with respect to bare Ti:Fe₂O₃, as a result of a decreased competition from OER. Despite the enhancement obtained by engineering the surface of the Ti:Fe₂O₃ photoanode with a tailored cocatalyst, the absolute FE is still far from ideal. A possible route to avoid OER competition would require the replacement of the reaction environment with a dry organic electrolyte, previously demonstrated by us to be compatible with PEC valorization reactions coupled to hydrogen evolution.^[24] However, preliminary results in this direction (Figure S12, Table S2, Supporting Information) displayed negligible HMF conversion to FDCA, being mainly DFF and by-products the only outcome of the reaction. This not only suggests the fundamental role of a basic aqueous media in establishing the hydration equilibrium of the aldehydes (Figure S8, Supporting Information), from which the last oxidation step to carboxylic acid takes place,^[33] but also highlights the importance of optimizing FE and selectivity in such reaction environment.

2.4. Optimization of FDCA Production

The previously described experiments show that the best photoanode for HMF photooxidation is Ti:Fe₂O₃-CoPi, but complete conversion of HMF to FDCA was not achieved. Indeed, even in the presence of a thick layer of CoPi cocatalyst, water oxidation is still a strongly competing process, negatively affecting the Faradaic efficiency for HMF oxidation, in particular in the low concentration range employed for HMF.

Based on the hypothesis that a limiting factor is constituted by mass transport of TEMPO to the photoanode surface (which is not a problem in the case of water, as it is the solvent), we performed experiments in saturated TEMPO (≈60 mM) borate buffer solution (0.25 M, pH 9.2) with Ti:Fe₂O₃ and Ti:Fe₂O₃-CoPi photoanodes. Under these experimental conditions, complete conversion of HMF to FDCA was achieved at $Q_{100\%}$ both with and without CoPi, indicating that a higher concentration of TEMPO is beneficial for a more efficient competition with the OER, although practically not sustainable, nor economically viable in the process scale-up.

To overcome the mass transport limitation, we tested a reduced-volume cell (1.8 vs 23 mL, Figure S13, Supporting Information) for the photooxidation of HMF (≈6 mM) in borate buffer (0.25 M, pH 9.2) and in the presence of the standard TEMPO concentration used in this work (≈6.5 mM). Such experimental apparatus ensured highly efficient stirring of the entire electrolyte volume, granting improved mass transport during the conversion experiment. Comparison of bare Ti:Fe₂O₃ with Ti:Fe₂O₃-CoPi photoanodes showed that a remarkable 86% yield for FDCA production was obtained for the CoPi-modified electrode at $Q_{100\%}$, compared to 54% in the absence of CoPi (Table S3, Supporting Information). As highlighted by the comparison of the results of the present photoconversion experiments with the available literature in the field (Table S4, Supporting Information), Ti:Fe₂O₃-CoPi is achieving comparable performance to state-of-the art BiVO₄ photoanodes, in terms of selectivity toward HMF photoconversion to FDCA, and largely outperforms the performance previously reported for hematite-based photoanodes in mild basic aqueous environment (pH 9.2).

2.5. Mechanistic Description of Charge Transfer Kinetics

In order to gain a mechanistic insight into the enhanced selectivity of CoPi toward HMF oxidation to FDCA, we investigated the dynamics of photogenerated holes in bare Ti:Fe₂O₃ and Ti:Fe₂O₃-CoPi by intensity-modulated photocurrent spectroscopy (IMPS). The analysis of IMPS spectra was performed using a novel approach, named Lasso distribution of relaxation time (L-DRT), which enables an easy identification of charge separation and recombination processes and an evaluation of transfer and recombination rate at the semiconductor/electrolyte interface. Further information about this analysis is reported here.^[34] In order to study the role of CoPi in TEMPO-mediated HMF oxidation, we started from the analysis of the Gartner current J_G , i.e., the photogenerated current density that reaches the semiconductor/electrolyte interface. This quantity is mainly sensitive to bulk phenomena and, upon normalization by the intensity of

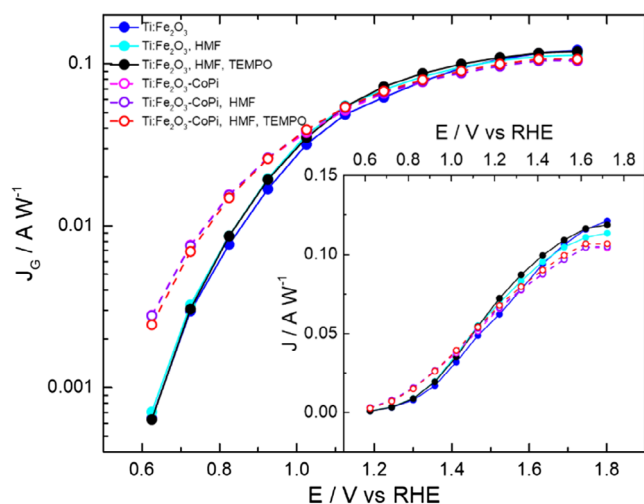


Figure 8. Gartner current J_G calculated using L-DRT algorithm and normalized by the intensity of incident light for Ti:Fe₂O₃ and Ti:Fe₂O₃-CoPi in borate buffer (0.25 M, pH 9.2) and in the presence of 2.5 mM HMF and 6.5 mM TEMPO.

the incident light, it represents the charge separation efficiency (CSE) multiplied by the light harvesting efficiency (LHE) of the system. **Figure 8** clearly shows that J_G remains almost constant upon addition of different species in the electrolyte for each electrode, while a strong variation is observed among the two photoanodes: the presence of CoPi induces a higher J_G at lower applied potential (<1.1 V vs RHE) and a slightly lower J_G at high potential when the dark current starts increasing.

This measurement suggests that CoPi promotes the accumulation of photogenerated charges at the semiconductor/electrolyte interface, enhancing charge separation especially at low potential. This finding is in agreement with the works by Hamman^[35] and Nellist,^[36] claiming CoPi that improves water splitting performance primarily by extracting photogenerated holes from hematite, confirming that CoPi acts as a hole-collecting layer and oxygen evolution catalyst.

As no effect related to the addition of HMF and TEMPO in solution is observed with respect to J_G , this has to be addressed

totally by the recombination current J_{rec} , which has opposite sign being generated by bulk-free electrons that reach the surface and recombine with trapped holes. As shown in **Figure 9**, bare Ti:Fe₂O₃ is typically characterized by a high J_{rec} , with a maximum at around 1.2 V versus RHE, caused by surface states recombination.^[37] The addition of HMF slightly mitigates this effect, decreasing the recombination peak in both bare Ti:Fe₂O₃ and CoPi, respectively, suggesting that HMF better intercepts the surface trapped photogenerated holes in presence of a CoPi overlayer. In addition, on average, the addition of CoPi on the surface of Ti:Fe₂O₃ leads to a 2x decrease in J_{rec} at low potential in the case of TEMPO addition, meaning that this oxidation pathway becomes more efficient.

According to IMPS theory,^[38] J_{rec} depends on the rate k^{tr} at which holes accumulated at the surface are transferred to the species in the electrolyte and on the rate k^{rec} at which they recombine with electrons from the bulk. As a consequence, in order to explain the behavior of J_{rec} , it is necessary to look at the transfer k^{tr} and k^{rec} rate. These parameters can be easily calculated using L-DRT in the whole potential range of these measurements. First of all, it is important to notice the strong dependence of both k^{tr} and k^{rec} on the applied potential (**Figure 10**), spanning over two orders of magnitude from 0.1 to 10 s⁻¹, since it is typical of bare hematite in aqueous solution (with only borate buffer) and indicates the presence of a high density of surface states that causes a metal-like behavior of its surface.^[37,39] Regarding the effects of the addition of HMF and TEMPO on k^{tr} and k^{rec} , we can notice that in bare Ti:Fe₂O₃ k^{tr} increases by about one order of magnitude upon the addition of HMF, going from 0.1 to 1 s⁻¹, and another order of magnitude, from 1 to 10 s⁻¹, with TEMPO, in the potential range between 0.8 and 1.2 V versus RHE (Figure 10a). In the same potential range, k^{rec} remains almost unaffected upon the addition of HMF and TEMPO (Figure 10b) and only above 1.2 V versus RHE the addition of TEMPO significantly reduces k^{rec} . This suggests that for bare Ti:Fe₂O₃ the decrease in J_{rec} highlighted in Figure 9a upon the addition of HMF and TEMPO can be mostly ascribed to the increase of k^{tr} . On the other hand, the addition of a CoPi layer on Ti:Fe₂O₃ reduces considerably the dependence of k^{tr} on the applied potential, regardless the presence of HMF and TEMPO.

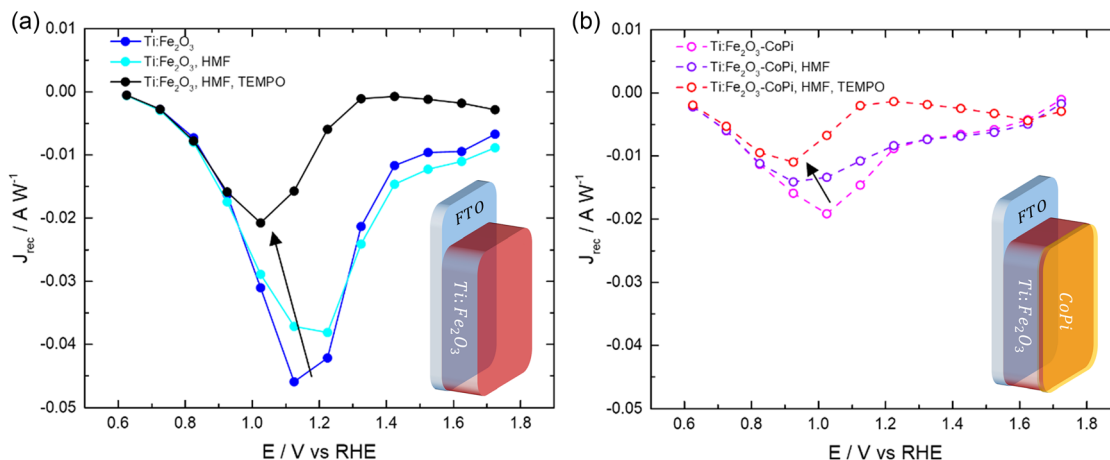


Figure 9. a) J_{rec} of Ti:Fe₂O₃ and b) Ti:Fe₂O₃-CoPi, in borate buffer (0.25 M, pH 9.2) and in the presence of 2.5 mM HMF and 6.5 mM TEMPO.

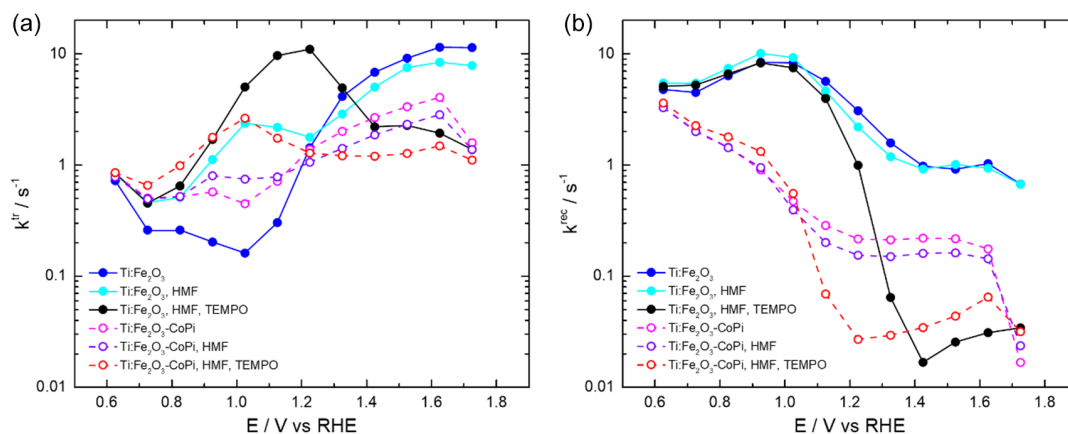


Figure 10. a) Transfer rate k^{tr} and b) recombination rate k^{rec} of Ti:Fe₂O₃ and Ti:Fe₂O₃-CoPi, in borate buffer (0.25 M, pH 9.2) and in the presence of 2.5 mM HMF and 6.5 mM TEMPO.

However, k^{rec} decreases by about one order of magnitude in the whole potential range (above 0.8 V vs RHE) after the addition of CoPi. As for bare Ti:Fe₂O₃, the addition of TEMPO reduces k^{rec} above 1.1 V versus RHE, meanwhile HMF has no effect on this rate constant. From these observations, it is possible to conclude that the decrease in J_{rec} after the addition of CoPi is mainly due to the suppression of recombination processes, i.e., to a decrease in k^{rec} , rather than an acceleration in transfer processes.

In order to corroborate the IMPS experiments, we addressed the capacitive response of the Ti-hematite interfaces by exploiting electrochemical impedance spectroscopy (EIS) on bare Ti:Fe₂O₃ and Ti:Fe₂O₃-CoPi. For EIS investigations, we focused on the response of these photoanodes in borate buffer, either in the presence or in the absence of TEMPO, acting as a fast (reversible) redox shuttle to mediate the photoelectrochemical oxidation of the organic substrates. In general, the stability of hematite during photoelectrochemical measurements (including the multi-voltage EIS investigations of the duration of several tens of minutes) was

satisfactory as shown by the J/V curves reported before and after EIS data collection (Figure S15, Supporting Information).

Excitation of hematite creates electrons and holes which can be transferred across the semiconductor under the influence of a reverse bias (anodic polarization) which controls the Fermi level of the semiconductor. Carriers (holes and electrons) can also be trapped in surface states which can act as recombination centers unless the electric field is strong enough to sweep the carriers in opposite directions, which will generate the photoanodic current described before. As a consequence, for Ti:Fe₂O₃, we have adopted a simple nested RC mesh used by us and by various authors^[40] to take into account the main dynamic processes following charge separation (Figure 11a). Charge transfer across the semiconductor is described by the R_{ct} - C_{sc} element where C_{sc} = constant phase element is a nonideal capacitance originated by a distribution of relaxation time constant, usual in porous interfaces of our interest. The R_{rec} - C_{ss} element describes recombination via trap states/surface states (interfacial

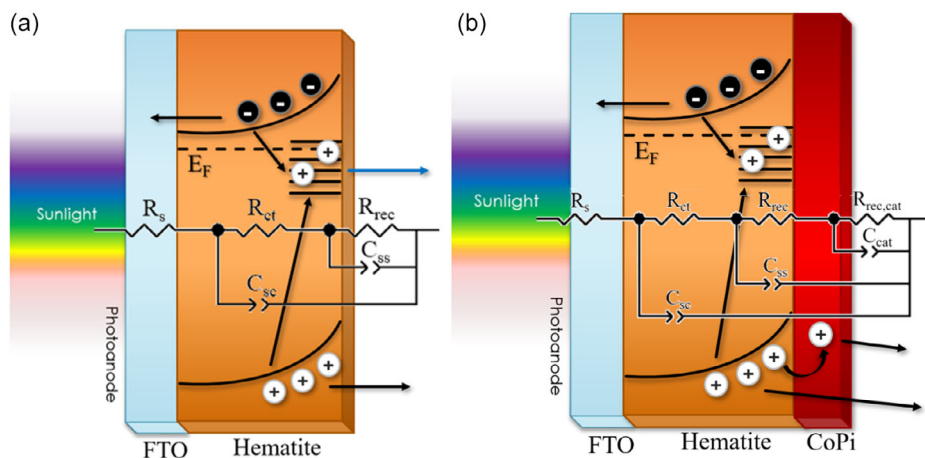


Figure 11. a) General charge transfer and recombination pathways in Ti:Fe₂O₃ electrodes and equivalent circuit used for fitting the EIS response. The FTO Ohmic contact is represented by the pale blue slab. Charge transfer to the electrolytic solution can occur through trapped and valence band holes (blue and black arrows). b) Ti:Fe₂O₃-CoPi electrode and the equivalent circuit to model the EIS response of such electrodes. C_{cat} is the constant phase element (CPE) modeling the chemical capacitance of CoPi.

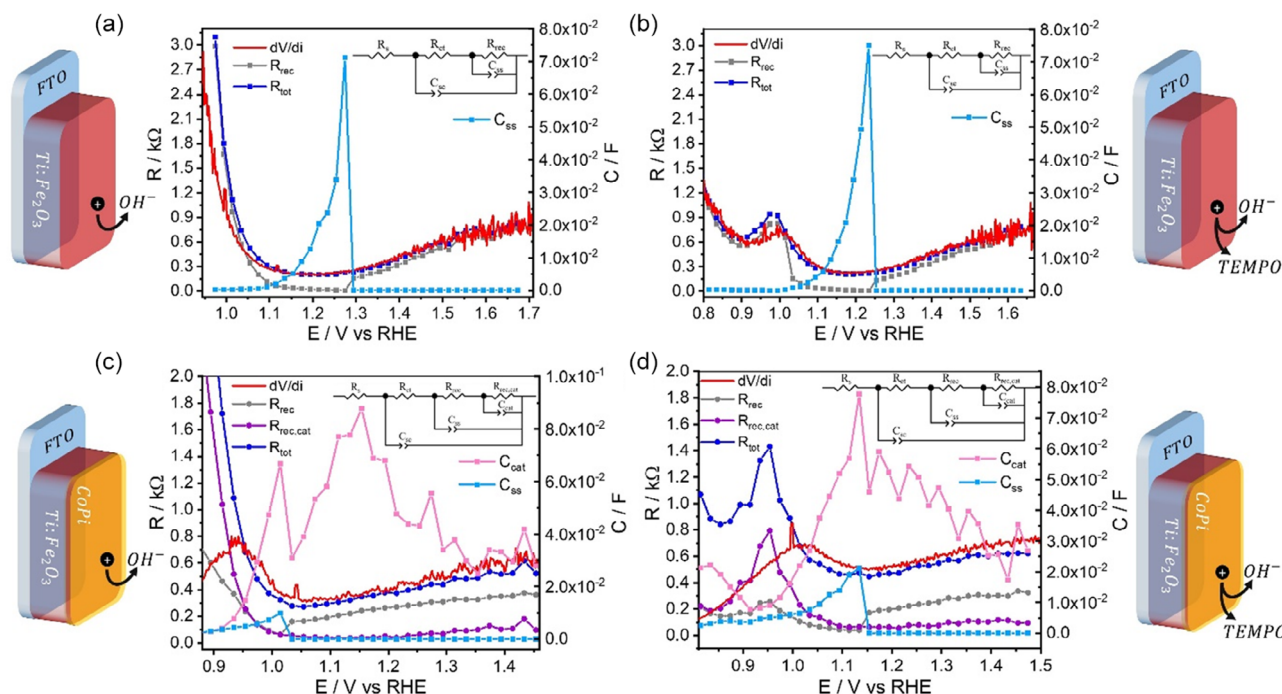


Figure 12. Resistive and capacitive contribution of $\text{Ti:Fe}_2\text{O}_3$ in a) borate buffer (0.5 M, pH 9.2) or b) with the addition of TEMPO (6.5 mM) to the electrolyte, extracted from EIS data fitting. c,d) Corresponding resistive and capacitive contribution for $\text{Ti:Fe}_2\text{O}_3\text{-CoPi}$.

recombination). R_s is the potential independent resistance, due to the contact and ohmic resistance of the electrolyte.

Fitting with the model above was generally successful in reproducing the J/V characteristics of the photoanode as shown by the good overlap of the computed points (blue squares in **Figure 12a**) with the reciprocal derivative of the J/V (red continuous line). We observe that the recombination resistance R_{rec} (gray squares) displays a minimum in correspondence to the chemical capacitance peak (cyan squares) due to C_{ss} , which describes the hole trapping capacitance and spans the interval between 1 and 1.3 V versus RHE, corresponding to inflection point of the respective J/V characteristics. When the applied bias is strong enough, electrons are swept to the back contact, and no longer recombine with trapped holes. Thus, the chemical capacitance peak (C_{ss}) disappears and the recombination resistance (R_{rec}) increases. The EIS analysis of $\text{Ti:Fe}_2\text{O}_3$ in the presence of 6.5 mM TEMPO (**Figure 12b**) outlines the same features described above, with an additional resistance peak associated to the reduction of TEMPO occurring around 0.9 V versus RHE at the $\text{Ti:Fe}_2\text{O}_3$ interface. The trapped hole capacitance peak displays an intensity similar to the previous case, but the inspection of the C_{ss} peak in the presence of TEMPO reveals a cathodic shift with respect to the previous case (**Figure S15**, Supporting Information), consistent with the shift observed in the J/V curves. This confirms that when TEMPO is present, a lower bias is needed to counter recombination and that TEMPO directly participates to a faster hole scavenging reaction at the $\text{Ti:Fe}_2\text{O}_3$ /electrolyte interface.

In the presence of CoPi, another nested RC element ($R_{\text{rec,cat}}\text{-}C_{\text{cat}}$) was inserted to model the charge transfer across the catalyst layer (**Figure 11b**). We postulate that transfer to the electrolyte through

CoPi occurs via surface states in hematite and that recombination resistances should add, since holes inside the CoPi layer become increasingly decoupled from electrons in the semiconductor. Fitting of the experimental data with such model affords the results in **Figure 12c**, which again show a good agreement between the total resistance (R_{tot} , blue dots) with the reciprocal derivative of the J/V curve (red line) above ≈ 1 V. The deviation at lower potentials is due to a dark faradaic process (visible in cyclic voltammograms, not shown here) assigned to either reduction of TEMPO or TEMPO oxidation by-products generated by the photoelectrochemical process. The plot of the capacitance reveals that the trapped hole density in $\text{Ti:Fe}_2\text{O}_3$ (C_{ss}) decreases by a factor of ≈ 10 , becoming marginal at voltages higher than 1.05 V versus RHE, whereas the CoPi-associated capacitance (C_{cat}) exhibits a broader distribution spanning the entire 0.9–1.5 V versus RHE interval, with an anticipated onset (≈ 0.9 V vs RHE) with respect to $\text{Ti:Fe}_2\text{O}_3$. This means that electron/hole separation in the CoPi-modified electrodes occurs at a lower bias than in $\text{Ti:Fe}_2\text{O}_3$, probably thanks to hetero-interfacial effects that increase the depletion field inside the semiconductor. The CoPi capacitance displays a peak centered around 1.15 V versus RHE, which represents the quasi-Fermi level reached by the catalyst under steady state illumination conditions. We also note that $R_{\text{rec,cat}}$ increases as the chemical capacitance of CoPi decreases, corroborating its assignment to the recombination resistance across CoPi. Finally, we observe that in the presence of TEMPO (**Figure 12d**), the EIS response is similar to **Figure 12c** in terms of resistance and chemical capacitance. Remarkably, however, the capacitance peak of CoPi significantly decreases, as better shown by the comparison in **Figure S18**,

Supporting Information. Moreover, the charge trapped in CoPi, obtained by integrating the respective capacitance curve, decreases by a factor of 2 when TEMPO is present ($\int 2(C_{\text{cat,TEMPO}}) \approx \int A(C_{\text{cat}})$), indicating that holes in CoPi are scavenged in a faster and more selective way by TEMPO. This is probably the key to understand the superior selectivity of Ti:Fe₂O₃-CoPi electrodes in TEMPO-catalyzed HMF oxidation. Indeed, the significantly decreased CoPi capacitance when TEMPO is used as electron shuttle points to a good selectivity of TEMPO oxidation, which can be usefully exploited for biomass oxidation.

3. Conclusion

The photoelectrochemical activity of Ti-modified hematite photoanodes was investigated towards the TEMPO-mediated oxidation of a biomass derivative (HMF) to a valuable compound (FDCA). The selectivity and the Faradaic efficiency of the PEC process were tuned by engineering the photoelectrode surface with the addition of Co-based cocatalysts films, namely CoPi and CoFeO_x films. While the presence of the latter cocatalyst produced a detrimental effect due to improved competition of OER, the addition of CoPi results in a significant improvement in terms of selectivity (86% yield for FDCA production, as compared to 54% of the bare hematite), as well as Faradaic efficiency. These results represent an important step forward with respect to the state of the art, as they were obtained on earth-abundant hematite photoanodes and in mildly basic aqueous environment (borate buffer, pH 9.2) compared to previously tested highly basic conditions,^[25] where HMF stability is poor and water reduction to hydrogen is highly disfavored. Moreover, the charge carrier dynamics investigation, performed by EIS and a newly introduced L-DRT algorithm for the analysis of IMPS spectra, shed light on the important role of the CoPi layer toward the suppression of recombination processes and the enhancement of hole transfer efficiency to TEMPO, positively affecting the catalytic process. Our work provides an extensive study on a promising anodic reaction performed by highly stable photoanodes, with the potential to be implemented in a tandem PEC cell, coupling the simultaneous reduction of H₂O or CO₂ at the cathode. Future efforts are envisioned toward the improvement of the cell setup to maximize mass transport of TEMPO, as well as the investigation of the economic and environmental impact resulting from the scale up of this appealing photosynthetic process.

4. Experimental Section

Materials: Chemicals and solvents were purchased from Merck, Alfa Aesar and Carlo Erba and were used as received. A Millipore system was exploited to produce deionized water used for material preparations.

Ti-modified Hematite Photoanodes Preparation: The photoanode fabrication and structural characterization were made by adapting and combining various previously reported synthetic approaches.^[41,42] Ti (IV)-modified nanostructured hematite photoanodes (Ti:Fe₂O₃) were prepared on a fluorine-doped SnO₂ (FTO) conductive glass by a hydrothermal approach. Briefly, the FTO glass was cleaned through ultrasonication in isopropanol and then rinsed with deionized water. The fabrication of hematite nanorod electrodes involved the deposition of a Ti (IV) modified iron oxide seed layer by dip coating (0.625 mm s⁻¹) the cleaned 2 mm thick FTO/glass

slides (10 mm (wide) × 25 mm (long)) in a Fe(III) oleate precursor containing 15 mm titanium (IV) isopropoxide in order to obtain a 10 mm × 10 mm coated area. The dip coating solution was prepared following the procedure described by D. K. Bora.^[41] The Fe(III) oleate layer was converted into hematite following a 30 min heat treatment at 500 °C. Solvothermal synthesis was carried out in a teflon-lined stainless steel autoclave by using an aqueous precursor containing 0.91 M sodium nitrate (NaNO₃, Carlo Erba Reagents), at a pH value of 1.5 adjusted with 6 M HCl, 0.136 M of ferric chloride (FeCl₃·6 H₂O, Alfa Aesar), 2.5 mM Ti₂CN (Sigma-Aldrich), and a 5% v/v ethanol (Carlo Erba Reagents).^[43] The seed-layered electrodes were inserted into the autoclave, lying at an angle of ≈45° with respect to the vertical liner walls. Heating at 95 °C was applied for 4 h. A uniform layer of yellowish color film (FeOOH) was formed on the electrodes. The FeOOH-coated substrates were washed with deionized water to remove weakly interacting residues from the hydrothermal bath before sintering in air at 550 °C for 1 h, during which conversion of FeOOH to Fe₂O₃ occurred. Finally, the resulting hematite thin films were modified by chemical bath treatment in a 0.2 M TiCl₄ solution heated at 50 °C for 1 h, followed by a final thermal annealing at 760 °C for 10 min affording the Ti:Fe₂O₃ electrodes used for this study.

Cocatalysts Modification of Ti-Hematite Photoanodes: The deposition of cobalt phosphate (Co₃(PO₄)₂, referred to as CoPi) on hematite electrodes using the electrodeposition method was according to directions from by Kanan and Nocera.^[29] Briefly, deposition was performed in a three electrode cell containing a solution of 0.5 mM cobalt(II) nitrate (Co(NO₃)₂·6H₂O) and potassium phosphate (0.1 M KH₂PO₄ at pH 7.0) using a SCE as reference electrode, hematite as working and a Pt foil as counter electrode. CoPi was electrodeposited applying the potential at which we recorded 0.322 mA cm² during a dark linear sweep voltammetry. The desired current values are usually recorded at around 1.1 V versus SCE. In order to obtain a thick CoPi layer over the hematite film, the potentiostatic electrolysis was carried out for ≈30 min corresponding to ≈530 mC cm² of passed charge (Figure S18, Supporting Information).

CoFeO_x deposition was accomplished by adapting a previous method outlined by Liardet et al.^[30] An aqueous solution containing 1.6 mM cobalt(II) chloride (CoCl₂·6H₂O) and 0.5 mM iron(III) sulfate (Fe₂(SO₄)₃·5H₂O) was prepared in 0.1 M sodium acetate (CH₃COONa). The hematite substrate was immersed in the as-prepared solution, and the deposition of CoFeO_x was performed by 10 s chronoamperometry at 600 mV versus SCE, by back illuminating the hematite electrodes under AM 1.5G conditions. SCE was the reference electrode, and a Pt foil was used as the counter electrode. The total amount of charge passed during the photoelectrodeposition was about 4 mC cm² (Figure S19, Supporting Information).

Structural and Optical Characterization: SEM images were collected on a Zeiss LEO 1430 FE-SEM. HR-TEM and scanning transmission electron microscopy (STEM-HAADF) characterization were performed on a FEI Tecnai F20, operating at 200 kV, and equipped with EDAX Phoenix spectrometer with ultrathin window detector for EDS.

X-ray diffraction (XRD) patterns were recorded employing a PANalytical X'Pert Pro automated diffractometer equipped with an X'celerator multielement solid-state detector. The diffractometer was operated in Bragg-Brentano $\theta/2\theta$ para-focusing geometry using Ni-filtered Cu K α radiation.

Optical transmittance was measured using an Osram 150 W xenon arc lamp coupled with a monochromator (Oriel Instruments) and a Si photodiode (Hamamatsu).

Photoelectrochemical Characterization: The three photoanodes were characterized in a custom-built PEEK two-compartments cell (Vol = 23 mL). The two compartments of the cells were separated by a Nafion membrane (N-117, thickness 0.007 in.). Each time, one of the hematite-based photoanode, i.e., Ti:Fe₂O₃, Ti:Fe₂O₃-CoPi, and Ti:Fe₂O₃-CoFeO_x, was used as the working electrode with Ag/AgCl (NaCl 3 M) as the reference electrode and platinum in the other compartment as the counter electrode. A borate buffer solution (0.25 M, pH 9.2) was used as the electrolyte. Chopped LSVs and CVs were performed using a Gamry Interface 1010E potentiostat. For the measurements under illumination, a simulated 1 sun-equivalent LED source was employed (Seoul

semiconductors Sunlike LED). The illumination of the working electrodes was achieved from the back side, through the fluorine-doped tin oxide (FTO) that is the substrate on which the Ti:Fe₂O₃ was deposited. The white LED was calibrated to reach, approximately, the power density of 100 mW cm⁻² at the surface of the FTO (before light penetrates FTO), by using a multimeter and a reference solar cell. Chopped LSVs were conducted by sweeping the potential to the positive direction at a scan rate of 50 mV s⁻¹ (step size: 2 mV), at room temperature and without stirring. CVs were performed in the same conditions, by first scanning the potential to the positive direction. Although the working electrode potentials were measured against an Ag/AgCl (NaCl 3 M) reference electrode, all the results are reported against the RHE, to make the comparison easier with H₂O/O₂ redox levels and with other reports that used other electrolytes at different pH. To do this conversion, Nernst Equation (2) was applied

$$E(\text{vs RHE}) = E(\text{vs Ag/AgCl}) + E_{(\text{Ag/AgCl})}^0 + 0.059 \cdot \text{pH} \quad (2)$$

where $E_{(\text{Ag/AgCl})}^0 = 0.205\text{V}$ versus NHE at 25°C

HMF and FFCA Photoconversion: A two-compartment PEEK cell or a reduced-volume cell (Figure S13, Supporting Information) was used for the bulk electrolysis experiments. Borate buffer solutions (0.25 M, pH 9.2) containing TEMPO (6.5 or 60 mM), FFCA (6.5 mM), or HMF (2.5 or 6 mM) were used. Pulsed chrono-coulometries were conducted under continuous stirring, at +0.9 V versus Ag/AgCl (= 1.6 V vs RHE) with a frequency of 1.6 mHz. To monitor the reaction, the solution was sampled over time. The samples taken from the solution were then analyzed, to quantify the oxidation products and to calculate their respective yields and FEs.

For the HMF photoconversion experiments, HPLC-electrospray ionization mass spectra and chromatographs were obtained with an Agilent Technologies MSD1260 Infinity II with single-quadrupole mass spectrometer and an isocratic elution with aqueous ammonium formate (5 mM): MeOH (ratio 7:3), using a reverse phase 25 cm Luna Omega C-18 column. The flow rate was 0.5 mL min⁻¹. The injected volume was 2 μL of the pristine undiluted sample. Identification and computation of the concentration of the compounds were obtained by calibration curves on chromatograph peaks (from the absorption recorded by diode-array detectors at 254, 280, and 310 nm) using solutions of known concentrations (ranging from 0.1 to 10 mM) of commercial standards. The retention times were 4.4 min for FDCA, 5.5 min for FFCA, 8.1 min for HMF, and 9.2 min for DFF.

Photophysical measurements were carried out in water at 298 K. UV–visible absorbance spectra were recorded with a Perkin Elmer λ650 spectrophotometer, using quartz cells with a 1.0 cm path length. The estimated experimental error is 5% on the molar absorption coefficients.

EIS and IMPS Measurements: The electrochemical impedance response of the illuminated photoanodes was carried out by applying a 10 mV sinusoidal perturbation in the $2 \times 10^4 - 5 \times 10^{-2}$ Hz, by using an EcoChemie FRA2 frequency response analyzer. The current/voltage characteristic of each photoanode was sampled at 20 mV intervals from the OCP to the limiting photocurrent plateau. Fitting of EIS data in terms of electric equivalents was achieved with Zview with typical relative errors <10%.

IMPS spectra of the photoanodes were measured in a PEEK cell with a PGSTAT204 electrochemical workstation, using a three-electrode configuration with a Pt counter electrode and an Ag/AgCl electrode as the reference. The electrolyte was a borate buffer solution (0.25 M, pH 9.2). IMPS measurements were performed in the applied bias range of 0.5–1.7 V versus RHE and frequency range of 0.1 Hz to 10 kHz. A monochromatic LED, with nominal wavelengths of 470 nm, was driven by a LED driver (Thorlabs DC2100) to superimpose a modulated illumination to a constant illumination bias. The sinusoidal modulation was about 10% of the DC illumination bias (4 mW cm⁻²), to ensure a linear response of the LED. Using a beam splitter, the light was divided into two beams, one on the PEC cell to illuminate the sample, and the other one on a calibrated Si photodiode (Hamamatsu) to measure the light intensity.

Supporting Information

Supporting Information is available from the Wiley Online Library or from the author.

Acknowledgements

This project has received funding from the European Union's Horizon 2020 research and innovation program under grant agreement No 101006839 (CONDOR). S.G. gratefully acknowledges funding from PON Ricerca e Innovazione (S.G.) 2014-2020. Caterina Bellatreccia is gratefully acknowledged for support with some photoelectrochemical experiments.

Conflict of Interest

The authors declare no conflict of interest.

Data Availability Statement

The data that support the findings of this study are available from the corresponding author upon reasonable request.

Keywords

biomass valorization, intensity-modulated photocurrent spectroscopy, photoelectrochemistry, α-Fe₂O₃

Received: May 9, 2023

Revised: June 9, 2023

Published online:

- [1] Z. Wang, C. Li, K. Domen, *Chem. Soc. Rev.* **2019**, *48*, 2109.
- [2] Y. H. Chiu, T. H. Lai, M. Y. Kuo, P. Y. Hsieh, Y. J. Hsu, *APL Mater.* **2019**, *7*, 080901.
- [3] D. K. Dogutan, D. G. Nocera, *Acc. Chem. Res.* **2019**, *52*, 3143.
- [4] I. Roger, M. A. Shipman, M. D. Symes, *Nat. Rev. Chem.* **2017**, *1*, 0003.
- [5] T. Gatti, F. Lamberti, R. Mazzaro, I. Kriegel, D. Schlettwein, F. Enrichi, N. Lago, E. Di Maria, G. Meneghesso, A. Vomiero, S. Gross, *Adv. Energy Mater.* **2021**, *11*, 2101041.
- [6] H. Song, S. Luo, H. Huang, B. Deng, J. Ye, *ACS Energy Lett.* **2022**, *7*, 1043.
- [7] A. Y. Ru Ng, B. Boruah, K. F. Chin, J. M. Modak, H. Sen Soo, *ChemNanoMat* **2020**, *6*, 185.
- [8] J. P. Barham, B. König, *Angew. Chem. Int. Ed.* **2020**, *59*, 11732.
- [9] L. Zhang, L. Liardet, J. Luo, D. Ren, M. Grätzel, X. Hu, *Nat. Catal.* **2019**, *2*, 366.
- [10] S. Bhattacharjee, V. Andrei, C. Pornrunroj, M. Rahaman, C. M. Pichler, E. Reisner, *Adv. Funct. Mater.* **2021**, *32*, 2109313.
- [11] T. Uekert, H. Kasap, E. Reisner, *J. Am. Chem. Soc.* **2019**, *141*, 15201.
- [12] H. Zhou, Y. Ren, Z. Li, M. Xu, Y. Wang, R. Ge, X. Kong, L. Zheng, H. Duan, *Nat. Commun.* **2021**, *12*, 4679.
- [13] T. Uekert, M. F. Kuehnell, D. W. Wakerley, E. Reisner, *Energy Environ. Sci.* **2018**, *11*, 2853.
- [14] X. Wu, X. Fan, S. Xie, J. Lin, J. Cheng, Q. Zhang, L. Chen, Y. Wang, *Nat. Catal.* **2018**, *1*, 772.
- [15] Y. Choi, R. Mehrotra, S.-H. Lee, T. V. T. Nguyen, I. Lee, J. Kim, H. Yang, H. Oh, H. Kim, J. Lee, Y. H. Kim, S.-Y. Jang, J. Jang, J. Ryu, *Nat. Commun.* **2022**, *13*, 5709.

- [16] M. Ko, L. T. M. Pham, Y. J. Sa, J. Woo, T. V. T. Nguyen, J. H. Kim, D. Oh, P. Sharma, J. Ryu, T. J. Shin, S. H. Joo, Y. H. Kim, J. W. Jang, *Nat. Commun.* **2019**, *10*, 5123.
- [17] T. Werpy, G. Petersen, *Us Nrel* 2004, Medium: ED; Size: 76 pp. pages.
- [18] H. G. Cha, K. S. Choi, *Nat. Chem.* **2015**, *7*, 328.
- [19] D. J. Chadderton, L. Wu, Z. A. McGraw, M. Panthani, W. Li, *ChemElectroChem* **2019**, *6*, 3387.
- [20] C. R. Lhermitte, N. Plainpan, P. Canjura, F. Boudoire, K. Sivula, *RSC Adv.* **2020**, *11*, 198.
- [21] EC, *Critical Raw Materials Resilience: Charting a Path Towards Greater Security and Sustainability* **2020**.
- [22] Y. Piekner, D. S. Ellis, D. A. Grave, A. Tsyganok, A. Rothschild, *Energy Environ. Sci.* **2021**, *14*, 4584.
- [23] J. Li, D. Chu, *Multifunctional Photocatalytic Materials for Energy* **2018**, p. 49, <https://doi.org/10.1016/B978-0-08-101977-1.00005-3>.
- [24] R. Mazzaro, S. Boscolo Bibi, M. Natali, G. Bergamini, V. Morandi, P. Ceroni, A. Vomiero, *Nano Energy* **2019**, *61*, 36.
- [25] A. Kawde, M. Sayed, Q. Shi, J. Uhlig, T. Pullerits, R. Hatti-Kaul, *Catalysts* **2021**, *11*, 969.
- [26] K. R. Vuyyuru, P. Strasser, *Catal. Today* **2012**, *195*, 144.
- [27] J. Zhang, R. García-Rodríguez, P. Cameron, S. Eslava, *Energy Environ. Sci.* **2018**, *11*, 2972.
- [28] D. K. Zhong, D. R. Gamelin, *J. Am. Chem. Soc.* **2010**, *132*, 4202.
- [29] M. W. Kanan, D. G. Nocera, *Science* **2008**, *321*, 1072.
- [30] L. Liardet, J. E. Katz, J. Luo, M. Grätzel, X. Hu, *J. Mater. Chem. A* **2019**, *7*, 6012.
- [31] S. Berardi, J. Kopula Kesavan, L. Amidani, E. M. Meloni, M. Marelli, F. Boscherini, S. Caramori, L. Pasquini, *ACS Appl. Mater. Interfaces* **2020**, *12*, 47435.
- [32] C. C. L. McCrory, S. Jung, J. C. Peters, T. F. Jaramillo, *J. Am. Chem. Soc.* **2013**, *135*, 16977.
- [33] P. Galletti, M. Pori, F. Funicello, R. Soldati, A. Ballardini, D. Giacomini, *ChemSusChem* **2014**, *7*, 2684.
- [34] A. Piccioni, P. Vecchi, L. Vecchi, S. Grandi, S. Caramori, R. Mazzaro, L. Pasquini, *J. Phys. Chem. C* **2023**, *127*, 7957.
- [35] B. Klahr, S. Gimenez, F. Fabregat-Santiago, J. Bisquert, T. W. Hamann, *J. Am. Chem. Soc.* **2012**, *134*, 16693.
- [36] M. R. Nellist, F. A. L. Laskowski, J. Qiu, H. Hajibabaei, K. Sivula, T. W. Hamann, S. W. Boettcher, *Nat. Energy* **2018**, *3*, 46.
- [37] L. M. Peter, K. G. U. Wijayantha, A. A. Tahir, *Faraday Discuss.* **2012**, *155*, 309.
- [38] E. A. Ponomarev, L. M. Peter, *J. Electroanal. Chem.* **1995**, *396*, 219.
- [39] B. Klahr, S. Gimenez, F. Fabregat-Santiago, T. Hamann, J. Bisquert, *J. Am. Chem. Soc.* **2012**, *134*, 4294.
- [40] P. Dias, L. Andrade, A. Mendes, *Nano Energy* **2017**, *38*, 218.
- [41] D. K. Bora, *Mater. Sci. Semicond. Process.* **2015**, *31*, 728.
- [42] J. Deng, J. Zhong, A. Pu, D. Zhang, M. Li, X. Sun, S. T. Lee, *J. Appl. Phys.* **2012**, *112*, 084312.
- [43] Y. Ling, G. Wang, D. A. Wheeler, J. Z. Zhang, Y. Li, *Nano Lett.* **2011**, *11*, 2119.